University of Reading

Large contribution of supercooled liquid clouds to the solar radiation budget of the Southern Ocean

Article

Published Version

www.reading.ac.uk/centaur

Large Contribution of Supercooled Liquid Clouds to the Solar Radiation Budget of the Southern Ocean

A. BODAS-SALCEDO, P. G. HILL, K. FURTADO, K. D. WILLIAMS, P. R. FIELD,
J. C. MANNERS, AND P. HYDER

Met Office Hadley Centre, Exeter, United Kingdom

S. KATO

NASA Langley Research Center, Hampton, Virginia

ABSTRACT

The Southern Ocean is a critical region for global climate, yet large cloud and solar radiation biases over the Southern Ocean are a long-standing problem in climate models and are poorly understood, leading to biases in simulated sea surface temperatures. This study shows that supercooled liquid clouds are central to understanding and simulating the Southern Ocean environment. A combination of satellite observational data and detailed radiative transfer calculations is used to quantify the impact of cloud phase and cloud vertical structure on the reflected solar radiation in the Southern Hemisphere summer. It is found that clouds with supercooled liquid tops dominate the population of liquid clouds. The observations show that clouds with supercooled liquid tops contribute between 27% and 38% to the total reflected solar radiation between 40° and 70°S, and climate models are found to poorly simulate these clouds. The results quantify the importance of supercooled liquid clouds in the Southern Ocean environment and highlight the need to improve understanding of the physical processes that control these clouds in order to improve their simulation in numerical models. This is not only important for improving the simulation of present-day climate and climate variability, but also relevant for increasing confidence in climate feedback processes and future climate projections.

1. Introduction

Clouds are major controllers of the top of the atmosphere (TOA) and surface energy budgets, and therefore play a leading role in determining the air–surface interaction that controls the evolution of important climate variables (Gregory and Morris 1996; Bennartz et al. 2013). Large solar radiation biases present in climate models over the Southern Ocean are largely associated with a poor simulation of low- and midlevel clouds (Williams et al. 2013; Bodas-Salcedo et al. 2012, 2014). They may also affect tropical atmospheric circulations and precipitation patterns (Ceppi et al. 2012; Hwang and Frierson 2013). Recent observational studies show the prevalence of supercooled liquid water ($T < 273.15\,\mathrm{K}$) in low-level clouds in the midlatitude oceans (Hu et al. 2010; Huang et al. 2012), but their simulation in climate models is still challenging (Cesana et al. 2012; Forbes and Ahlgrimm 2014). Their impact on Earth's radiation budget, although potentially significant (Hogan et al. 2003), is poorly understood over large regions and has not been quantified. In addition to their importance for present-day simulations, cloud-phase radiative feedbacks also dominate the cloud changes in the high latitudes (Senior and Mitchell 1993; Tsushima et al. 2006). The effect of these clouds on the radiative biases detected in climate models can be better understood by quantifying their contribution to the radiation budget.

Bodas-Salcedo et al. (2014) analyze the shortwave (SW) reflected radiation model errors according to cloud regimes. The cloud regimes are defined using the cloud clustering algorithm developed by Williams and

Corresponding author address: A. Bodas-Salcedo, Met Office Hadley Centre, FitzRoy Road, Exeter, EX1 3PB, United Kingdom.
E-mail: alejandro.bodas@metoffice.gov.uk

Webb (2009), applied to model data from phase 5 of the Coupled Model Intercomparison Project (CMIP5; Taylor et al. 2012) and observations from the International Satellite Cloud Climatology Project (ISCCP; Rossow and Schiffer 1999). Using additional information from the *Cloud–Aerosol Lidar and Infrared Pathfinder Satellite Observations* (*CALIPSO*) satellite (Winker et al. 2009), they show that the ISCCP cloud clusters contain large internal variability in cloud vertical structure. This is particularly acute for the so-called midlevel cloud regime, which is the cloud cluster that contributes most to the model biases. One of the aims of this study is to provide a more direct connection between cloud vertical structure and reflected shortwave radiation. Given the recently observed prevalence of supercooled liquid water over the Southern Ocean, and the fact that cloud microphysical processes are especially challenging to models, a second aim is to quantify the contributions of cloud phase to the shortwave radiation budget.

Our ability to observe the vertical structure of clouds has been greatly enhanced in the last decade with the availability of two active instruments on board the *CloudSat* and *CALIPSO* satellites, flying in formation as part of the A-Train (Stephens et al. 2002). These instruments have been recently used to estimate the climatological impact of clouds on the atmospheric radiative heating (L'Ecuyer et al. 2008; Haynes et al. 2013). Here we use satellite data and radiative transfer simulations to quantify the contributions of different cloud types and cloud thermodynamic phase to the TOA radiation budget. We also analyze data from the most recent multimodel ensemble simulations to understand the implications of the present-day biases observed in the current generation of models over the Southern Ocean. We restrict our analysis to the austral summer season as our main focus in this study is in the solar part of the spectrum.

The paper is structured as follows. Section 2 describes the satellite data, the radiative transfer calculations, the model simulations, and the cyclone compositing methodology. This section also considers the implications of the uncertainty in the cloud-top phase identification. Section 3 presents the main results of the study, and section 4 summarizes the main conclusions and discusses future work.

2. Data and methodology

a. Satellite data

The combined CERES–*CloudSat*–*CALIPSO*–MODIS (CCCM) dataset (Kato et al. 2010, 2011) provides information on the vertical occurrence of clouds and their radiative properties. The Clouds and the Earth's Radiant Energy System (CERES) instruments measure the solar reflected and thermally emitted radiances at the top of the atmosphere. Fluxes are then obtained by applying an empirical angular distribution model (Loeb et al. 2005). Although the CERES fluxes are not direct measurements, we still use this terminology to distinguish between the CERES estimates and the fluxes obtained from radiative transfer calculations. The CERES radiometers have a horizontal resolution of 20 km at nadir. Two CERES instruments fly on board the *Aqua* satellite, in tight formation with the *CloudSat* and *CALIPSO* satellites, as part of the A-Train (Stephens et al. 2002). The Moderate Resolution Imaging Spectroradiometer (MODIS) is also on board the *Aqua* satellite. These four instruments observe the same scene within a few tens of seconds difference. The Cloud Profiling Radar (CPR) on board *CloudSat* and the Cloud–Aerosol Lidar with Orthogonal Polarization (CALIOP) on board *CALIPSO* provide information on the vertical distribution of clouds, and MODIS gives information on vertically integrated properties. Data from these three instruments are used to provide cloud radiative properties and thermodynamic phase. The CCCM dataset collocates information from these three instruments with radiation measurements from the CERES instrument. The number of cloud profiles in a CERES footprint can be as many as 50. For each CERES footprint (instrument with the coarsest resolution), CCCM defines up to 16 "cloud groups." A cloud group is a set of vertical profiles within a CERES footprint that share the same vertical distribution of clouds (i.e., that have the same cloud boundary heights). They can be single radar–lidar columns, but they are generally not. It is a way of reducing data volumes without losing too much spatial variability information within the CERES field of view (FOV). When the number of unique cloud groups exceeds 16, profiles with nearly the same cloud-top and cloud-base heights are combined. The vertical profile grouping process is detailed in Kato et al. (2010). For each of these cloud groups, cloud properties are reported with an approximate vertical resolution of 240 m. We use release B1 of the CCCM dataset, and Table 1 provides a list of the variables that are used in this study. We also use the 2000–13 climatology of TOA radiative fluxes from the CERES–Energy Balanced and Filled (EBAF) Ed2.8 dataset for comparisons with model simulations (Loeb et al. 2009).

Vertical profiles of cloud liquid and ice water content (IWC and LWC, variables CCCM-85 and -86) are derived in six steps. For each cloud group of which cloud-top and cloud-base heights are derived from *CALIPSO* and *CloudSat*, CCCM assigns a vertically constant extinction coefficient computed from the MODIS-derived cloud optical thickness, particle size, and phase for all overlapping layers. If *CloudSat*-derived IWC or LWC is

TABLE 1. Variables from CCCM files used for the radiative transfer calculations. CCCM files also include variables from the single satellite footprint (SSF) CERES files. The left column gives the SSF or CCCM index that uniquely identifies the variable. The right column shows the variable names as they appear in the CCCM files. The names are not fully descriptive. For instance, MODIS cloud phase is derived from the 3.7-, 11-, and 12-μm channels, as detailed in Minnis et al. (2011), not from a single channel.

Variable	Name
SSF-25	Surface type index
SSF-38	CERES SW TOA flux–upward
SSF-50	CERES broadband surface albedo
SSF-59	Surface skin temperature
SSF-97	Mean cloud effective temperature for cloud layer
SSF-107	Mean cloud particle phase for cloud layer (3.7 μm)
CCCM-11	Total number of good *CALIPSO* profiles
CCCM-12	Cloud group area percent coverage
CCCM-13	Cloud layer top-level height
CCCM-15	Cloud layer base-level height
CCCM-34	Mean group cloud particle phase from MODIS radiance (3.7 μm)
CCCM-76	Pressure profile
CCCM-77	Temperature profile
CCCM-78	Water vapor mixing ratio profile
CCCM-79	Ozone mixing ratio profile
CCCM-84	Cloud extinction coefficient profile used
CCCM-85	Liquid water content profile used
CCCM-86	Ice water content profile used

available, CCCM computes extinction coefficients due to ice particles or water particles for each cloud layer using *CloudSat*-derived cloud properties, and selects the one that gives a larger optical thickness for that layer. If *CALIPSO*-derived extinction is available, the extinction coefficient derived from MODIS or *CloudSat* is replaced by that derived from *CALIPSO*. Since *CALIPSO* is attenuated rapidly by water clouds, if the *CALIPSO* extinction profile is available, then CCCM assumes that the cloud is in the ice phase. CCCM integrates extinction coefficients vertically for each cloud group and normalize the total scaled optical thickness by the MODIS-derived scaled optical thickness. The scaled optical thickness is defined as $(1 - g)\tau$, where g is the asymmetry parameter and τ is the cloud optical thickness. Therefore, the scaled optical thickness for cloud groups is equal to the corresponding scaled optical thickness derived from MODIS. CCCM converts the extinction coefficient back to IWC and LWC vertical profiles for each cloud group, and averages them from all cloud groups, weighted by their cloud fractions within each CERES footprint. For this calculation, the *CALIPSO* or *CloudSat* estimates of effective radius are used if available. If not, the MODIS effective radius is used, assuming a constant particle size for the entire column. In summary, the *CALIPSO* extinction profile is used if

available, then *CloudSat* water content if *CALIPSO* extinction is not available, and MODIS if neither *CALIPSO* nor *CloudSat* profiles are available. CCCM ice and liquid water path, used for comparison with models in section 3, are calculated by vertically integrating the CCCM LWC and IWC.

b. Radiative transfer calculations

CCCM does not provide radiative fluxes for individual cloud groups, so we run the Edwards–Slingo (Edwards and Slingo 1996) radiative transfer code on each vertical profile that describes a CCCM cloud group. For each CERES footprint, a clear-sky calculation is also performed. We perform these calculations for five austral summers (December–February), from December 2006 to February 2011. Data for January 2011 are not available due to bad geolocation of *CloudSat* data, so a total of 420 days are processed. The calculations are restricted to the region between 40° and 72.5°S. The radiative transfer code requires profiles of pressure, temperature, water vapor, ozone, cloud water content (liquid and ice), and cloud particle effective dimensions (liquid and ice). CCCM provides cloud extinction (CCCM-84) and cloud liquid and ice water content for each level (CCCM-85 and -86), averaged over all the cloud groups. We calculate the cloud droplet effective radius as

$$R_e = \frac{3}{2}\text{CWC}\rho^{-1}\beta^{-1},$$

where CWC, ρ, and β are the condensate (liquid and/or ice) water content, density, and extinction coefficient, respectively. Both phases can coexist in the same cloud group, with independent optical properties. The effective radius is limited to a range between 4 and 30 μm for liquid and 5 and 150 μm for ice. We use the same values of water content and effective radius at each level for all cloud groups. This assumption effectively neglects the spatial variability of cloud properties in each layer. CCCM also provides information on the vertical profile of temperature (CCCM-77), pressure (CCCM-76), water vapor (CCCM-78), and ozone (CCCM-79), which come from the NASA Global Modeling and Assimilation Office (GMAO) Goddard Earth Observing System version 4 (GEOS4; Bloom et al. 2005) reanalysis before November 2007, and the GEOS and CERES (G5-CERES) reanalysis after that (Rienecker et al. 2008). Surface broadband albedo is also required as input (SSF-50).

CCCM also reports the fraction of the CERES footprint that is occupied by each cloud group (CCCM-12). We use the independent pixel approximation to estimate the radiative fluxes at CERES resolution by weighting each cloud group and clear-sky radiative
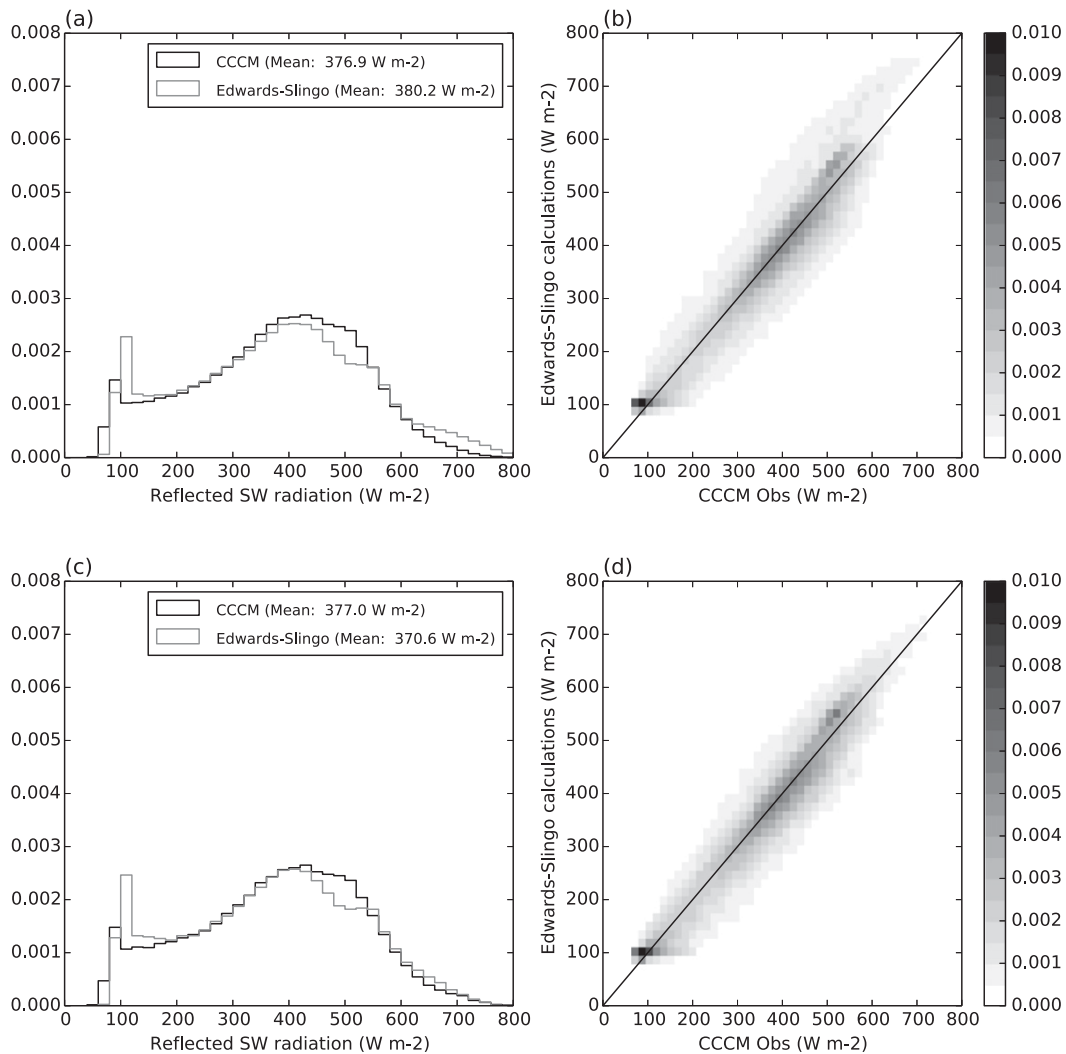
FIG. 1. Observed and simulated solar radiative fluxes over the Southern Ocean. (a) Frequency histograms of the instantaneous reflected solar radiation from the CCCM data (black) and the radiative transfer calculations (gray). (b) Density scatterplot of simulations (*y* axis) vs observations (*x* axis). (c),(d) As in (a),(b), but the radiative transfer calculations use the ice optical properties parameterization by Baran et al. (2013). Data from five DJF seasons (December 2006–February 2011) over the region 40°–72°S. The observations are instantaneous footprint measurements of the CERES instrument at the TOA. The simulations are run on all the cloud groups observed by the active instruments within each CERES footprint, and then weighted by the area fraction.

transfer calculations by their respective area fractions. We compare these estimates with the CERES measurements of the reflected solar radiation (SSF-38) to evaluate the accuracy of the methodology. The calculations are virtually unbiased, and the frequency distribution of the estimated fluxes compares well with the observed distribution (Fig. 1a), with some discrepancies in the low- and high-value ranges. The density plot in Fig. 1b reinforces the conclusion that the radiative transfer calculations perform reasonably well across the entire range of scenes. Large differences are observed in those CERES footprints with the largest fluxes (greater

than $550\,\mathrm{W\,m^{-2}}$), which correspond to thick clouds that tend to have glaciated tops. We have tested the impact of using different parameterizations of the ice optical properties that reduce the histogram differences for large values of reflected solar radiation. We use the parameterization by Kristjánsson et al. (1999) in our standard calculations (Figs. 1a,b). This is the parameterization used in the Met Office model at the time of writing. Figures 1c,d show the impact of replacing this standard parameterization with a newer parameterization (Baran et al. 2013). This newer parameterization reduces the biases, but the results and conclusions of this

study are robust with respect to the choice of ice optical properties parameterization.

The calculations overestimate the reflected solar radiation for dark scenes (i.e., clear skies or very thin clouds). Several causes may contribute to this bias: inaccurate surface albedo (SSF-50), wrong amount of shortwave absorbers or the parameterization of their radiative properties, or errors in scene identification (e.g., cloud fraction). The surface effect is taken into account in the radiative transfer calculations through the surface albedo. Apart from ocean, other two surface types have a significant population in the domain: permanent snow/ice and sea ice. Our calculations of TOA reflected fluxes are biased low over permanent snow, and biased high over sea ice. However, the populations of these two surface types are sufficiently small that the results shown in Fig. 1 are dominated by the ocean points.

The Southern Ocean is a region dominated by strong winds, which affect the surface albedo. We have also tested the sensitivity of our radiative transfer calculations to the surface wind speed. We have split the population in two halves according to wind speed, and both halves show very similar biases (not shown). We therefore conclude that the dependency of surface albedo with wind speed does not play a significant role in our analysis.

We have also investigated the causes of the differences in the range between 400 and 600 W m^{-2}. They are substantially reduced if CERES FOVs with total number of good *CALIPSO* profiles (CCCM-11) less than 50 are discarded. CERES FOVs with a small number of good *CALIPSO* profiles may introduce a low bias in cloud fraction that makes the radiative transfer calculations to be biased low. It is clear that errors in the cloud identification can introduce large errors in the radiative transfer simulations, and CALIOP plays a central role in the identification and retrieval of cloud properties. When CALIOP is not operational, the CCCM products rely on *CloudSat* to provide information on cloud top and base. However, *CloudSat* is not as sensitive to clouds as CALIOP. In particular, *CloudSat* is affected by ground clutter in the lower 800 m of the atmosphere (Marchand et al. 2008), which limits its ability to detect low-level liquid cloud. To reduce the amount of profiles with large errors in the inputs to our radiative transfer calculations, we discard from our analysis CERES FOVs when the following three conditions are met: CALIOP is not operational, the reported CERES footprint cloud fraction is smaller than 0.25, and the difference between the measured and estimated fluxes for the CERES footprint is larger than 100 W m^{-2}. The 100 W m^{-2} threshold is a conservative choice, so the results may still contain a small fraction of points affected by inputs with large errors. These three conditions have to be met at the

same time for rejection. The nonavailability of the *CALIPSO* lidar flags a higher risk of scene misidentification. We add two additional constraints to minimize the amount of points filtered out. Only 2% of the points are discarded. Although this may introduce some small biases, it is a better approach than keeping points with large scene identification errors that would introduce large spurious biases in the radiative transfer calculations.

c. Cloud-top phase identification

Huang et al. (2012, 2015) examine a variety of cloud phase products at high latitudes. While they find significant differences between products, they all show a large occurrence of supercooled liquid water over the southern oceans, with a large fraction of all liquid topped clouds being supercooled, in line with the results from earlier studies (Hu et al. 2010). To understand the sensitivity of our results to the uncertainties in cloud-top phase identification, we compare here results from three different methods. Our standard algorithm (referred to herein as method 1) uses the vertical profiles of temperature (CCCM-77), LWC (CCCM-85), and IWC (CCCM-86) in the uppermost cloud level of each cloud group. To understand the impact of the cloud-top phase identification in the results, we also use two additional algorithms. The second method (method 2) looks at each cloud group in a CERES footprint and uses the uppermost cloud-top water phase derived from MODIS (Minnis et al. 2011; CCCM-34). Because *CALIPSO*–*CloudSat* and MODIS are not necessarily seeing the same cloud, we only include points when cloud-top heights from *CALIPSO*–*CloudSat* and MODIS are within 1 km for high clouds (top > 6.5 km), within 0.5 km for midlevel clouds (6.5 ≥ top > 3.5 km), and within 0.2 km for low clouds (top ≤ 3.5 km). Method 3 uses a more conventional way of cloud-top phase identification. It uses MODIS only, which identifies one or two cloud layers in a CERES footprint and derives the water phase. Since several cloud layers can coexist within 20 km of a CERES footprint, more than one cloud-top height can be reported from MODIS. SSF and CCCM products include up to two nonoverlapping cloud-top heights in a CERES footprint (Minnis et al. 2011). Both cloud top phase (SSF-107) and cloud-top temperature (CTT; SSF-97) from MODIS are used. Any cloud that is classified as liquid and whose cloud-top temperature is below 0°C is then classified as supercooled. Methods 1 and 2 obtain the cloud-top temperature from the reanalysis temperature (CCCM-77) at cloud-top height. Method 3 uses the MODIS-derived cloud-top temperature (SSF-97). Table 2 summarizes the three methods.

TABLE 2. Summary of the three cloud-top phase identification methods. Cloud-top temperature (CTT) is used to distinguish between liquid and supercooled clouds.

	Method 1	Method 2	Method 3
Liquid	LWC > 0 and IWC = 0	CCCM-34 = 1	SSF-107 = 1
Ice	LWC = 0 and IWC > 0	CCCM-34 = 2	SSF-107 = 2
Mixed	LWC > 0 and IWC > 0	1 < CCCM-34 < 2	1 < SSF-107 < 2
CTT variable	CCCM-77	CCCM-77	SSF-97

The three methods give large differences in the probability of cloud-top phase identification (Fig. 2). However, the three methods are consistent with recent studies that show a large occurrence of supercooled liquid water over the southern oceans, with a large fraction of all liquid topped clouds being supercooled (Hu et al. 2010; Huang et al. 2015). The fractions of clouds (with respect to the total cloud fraction) with liquid tops between −40° and 0°C are 0.8, 0.84, and 0.60 respectively for the three methods. Total cloud fraction derived from MODIS is generally smaller than that derived from *CALIPSO–CloudSat*. Once thin clouds that are below detection limit of MODIS are excluded, cloud fractions agree to within 0.1 [see Fig. 11 of Kato et al. (2011)]. If only MODIS is used (method 3), it is difficult to screen thin ice clouds that might influence phase identification on lower-water clouds. This might be one of the reasons why method 3 shows smaller frequency of occurrence of supercooled water. If we restrict the lower temperature to −20°C, these fractions are 0.88, 0.86, and 0.67. Hu et al. (2010) estimate that, over the Southern Oceans, more than 85% of the clouds contain liquid phase for temperatures above −20°C. Our cloud-top phase classification method gives a comparable result for the average fraction of clouds with supercooled liquid tops. Figure 2 illustrates the current limits of remote observations of cloud-top thermodynamic phase. For instance, method 1 shows a much smaller liquid fraction for temperatures below −20°C compared to the other two methods, potentially due to the use of CCCM liquid and ice water content. Cloud retrievals based on passive imagers can also be affected by large biases, especially at large solar zenith angles (e.g., Grosvenor and Wood 2014). However, despite these uncertainties, the fact that all methods report large fractions of supercooled liquid for temperatures above −20°C gives robustness to the results presented below.

d. Model simulations

We use model simulations from the CMIP5 (Taylor et al. 2012). We analyze outputs from atmosphere-only experiments from 23 models: BCC_CSM1.1, BCC_CSM1.1(m), CCSM4, CESM1(CAM5), CNRM-CM5, CSIRO Mk3.6.0, CanAM4, FGOALS-s2, GFDL-HiRAM-C180, GFDL-HiRAM-C360, GISS-E2-R, HadGEM2-A, INM-CM4.0, IPSL-CM5A-LR, IPSL-CM5A-MR, IPSL-CM5B-LR, MIROC5, MPI-ESM-LR, MPI-ESM-MR, MRI-AGCM3.2H, MRI-AGCM3.2S, MRI-CGCM3, and NorESM1-M. (Expansions of model acronyms are available at http://www.ametsoc.org/PubsAcronymList.) The atmosphere-only experiments are run following the Atmospheric Model Intercomparison Project protocol (AMIP; Gates 1992). They use present-day boundary conditions and forcings: sea
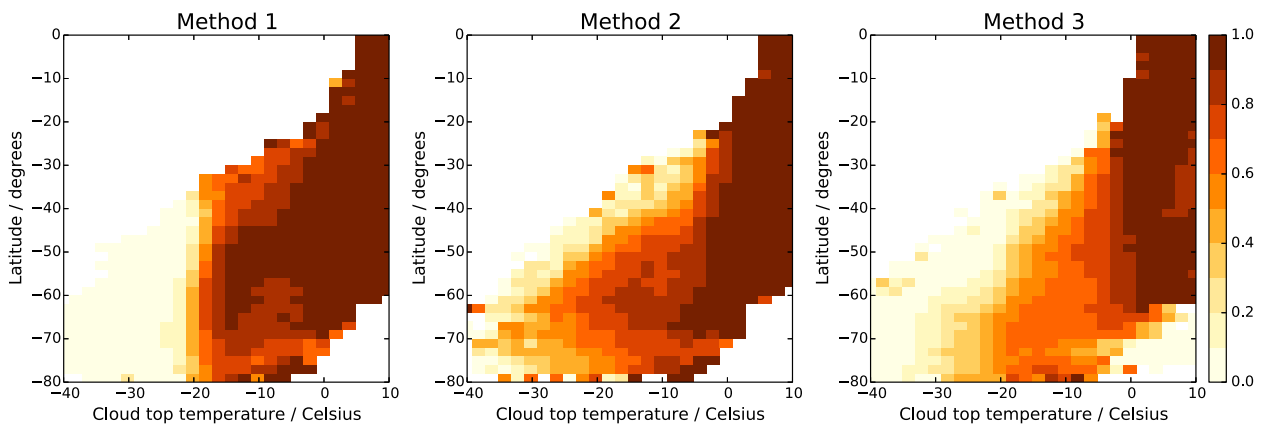

FIG. 2. Probability of liquid cloud tops relative to all clouds as function of latitude and cloud-top temperature for three different methods of cloud-top phase identification. Results are for the Southern Hemisphere.

surface temperatures (SSTs), sea ice, and greenhouse gases.

We also perform 2.2-km-resolution simulations of a Southern Ocean cyclone with a local-area configuration of the Met Office Unified Model. Two simulations were performed with heterogeneous ice nucleation occurring below $T_{nuc} = 0°C$ and $T_{nuc} = -40°C$, respectively. The simulations are performed over a $30° \times 30°$ area centered at 52°S, 0°E on 9 December 2014. The model fields where analyzed at 1-h intervals between 1100 and 1300 UTC, for a forecast initialized at 0000 UTC. Since we carry out a sensitivity experiment changing the heterogeneous freezing temperature, we give a brief description of the model's microphysical scheme here. The Unified Model microphysics is a single-moment bulk microphysics representation. It is based on Wilson and Ballard (1999), with extensive modifications (e.g., Abel et al. 2010). Liquid and ice mass mixing ratios are prognostics with explicit rate equations controlling the transfer of water between ice, liquid, and vapor phases. Loss of supercooled liquid can occur through evaporation, riming, and nucleation. Homogeneous freezing occurs at temperatures colder than $-40°C$ and freezes all of the water in the grid box. Heterogeneous freezing occurs for temperatures colder than $-10°C$ (in the operational configuration) and only when liquid water is present. This process seeds an amount of ice mass dependent on the temperature.

e. Cyclone compositing

We use the cyclone compositing methodology of Field and Wood (2007). Minima in daily mean sea level pressure are identified over the latitudes 40°–70°S. A box covering 60° in longitude and 30° in latitude is centered on the cyclone. This box is large enough that mature cyclones, and to some extent transient ridges ahead or behind the cyclone, can be included, but not so large to be seriously affected by a following large cyclone. Previous studies have found that two years of data give robust results. More details on this methodology are given in Field and Wood (2007) and Bodas-Salcedo et al. (2012).

3. Results

We use data from passive and active instruments from the A-Train (Stephens et al. 2002), and radiative transfer simulations to quantify the contribution of different cloud types to the radiation budget over the entire Southern Ocean. We process data for five Southern Hemisphere summers (December–February), from December 2006 to February 2011 (except January 2011 because of missing data). We classify each profile (or cloud group)

according to how the clouds are distributed in the vertical, following the cloud vertical structure (CVS) proposed by Tselioudis et al. (2013). The atmospheric column is divided into three layers, with pressure boundaries at 440 and 680 hPa. This follows the widely used division proposed by the ISCCP (Rossow and Schiffer 1999). The layers are labeled as follows: H for the high layer, M for the middle layer, and L for the low layer. A CVS is then a combination of the layers that contain cloud. For instance, the CVS labeled HM will contain profiles with clouds in the high and middle layers. Profiles in which a cloud extends across the pressure boundary between layers include an ''x'' between the layers' names. For instance, MxL contains cloud in the middle and low layers, with a cloud layer that extends across the 680-hPa pressure boundary. We also classify each profile by the cloud-top phase of the uppermost cloud layer (method 1 above). For each CVS, we have four phase categories: liquid (LIQ), supercooled liquid (SCL), mixed-phase (MIX), and ice (ICE). We also calculate statistics for clear-sky profiles (CLR). We calculate the area fraction of each combination of CVS and cloud-top phase, shown in the gray stacked histogram in Fig. 3a. The sum of all the bars is one. All the values quoted here are calculated over the population of CERES footprints analyzed. The Southern Ocean is covered with cloud around 87% of the time. This value is comparable to other (spatially complete) estimates, which reinforces the idea that the CERES FOV filtering is not introducing a significant selection bias. Profiles with only cloud in the lower (L) layer are the most frequent CVS, with one-third of the population. Low-, middle-, and high-top cloud account for 33%, 17%, and 37% of the cloud fraction, respectively. We use the radiative transfer simulations described above to quantify the contribution of each CVS–phase combination to the TOA shortwave radiation budget (color stacked histogram in Fig. 3a). The total radiative contribution of a CVS depends on its frequency of occurrence and on the average reflected flux when present. The sum of all the color bars gives a cloud-fraction and area-weighted average flux of $380 \, W \, m^{-2}$. This is not an estimate of the true climatological December–February (DJF) average because the temporal sampling is not homogeneous through the diurnal cycle. The main result from these calculations is that clouds containing supercooled liquid water at their tops contribute 30% of the total reflected flux, whereas clouds with ice, liquid, and mixed-phase tops contribute 45%, 11%, and 6%.

The distribution of cloud-top phase shows a latitudinal dependence (Fig. 3b). Supercooled liquid clouds show a maximum in occurrence between 60° and 65°S and are the most frequent category between 55° and
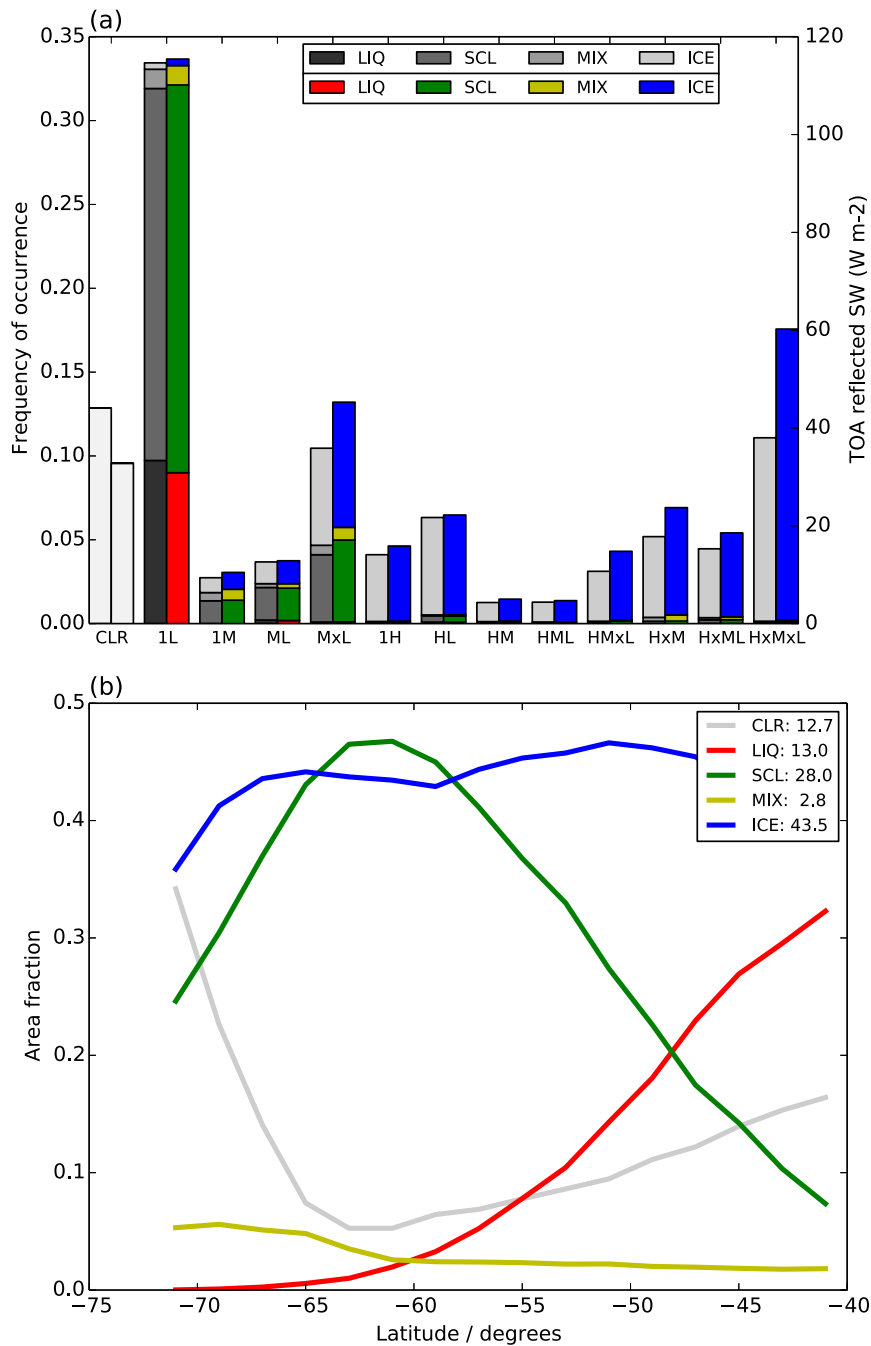
FIG. 3. Contribution of each cloud type and cloud thermodynamic phase to the solar radi-
ation budget over the Southern Ocean. (a) Vertical profiles are classified according to their
CVS and cloud-top phase. Clear profiles are labeled CLR. There are four cloud-top phase
classes: LIQ, SCL, MIX, and ICE. The gray bars show the average frequency of occurrence (left
y axis) for each CVS, partitioned by cloud-top phase. The colored bars show area-fraction-
weighted average of each CVS and phase combination (right y axis), which represents the
contribution of each CVS and phase to the total reflected flux. (b) Zonal-mean area fraction by
cloud-top phase. The area fraction of clear profiles is displayed in gray.

68°S. South of 60°S virtually all liquid clouds are super-cooled, and supercooled clouds dominate the population of liquid clouds poleward of 48°S. Ice clouds dominate the contribution to the TOA flux at all latitudes, except between 60° and 65°S, where supercooled liquid clouds lead the contribution to the TOA reflected flux.

It is worth mentioning that the identification of cloud top and cloud base in CCCM is primarily based on CALIOP-derived cloud profiles (Kato et al. 2010), which minimizes the impact of ground clutter in the *CloudSat* signal. When cloud base is not available from *CloudSat* and CALIOP is completely attenuated, the CALIOP lowest unattenuated base is chosen. The optical thickness for cloud groups is scaled to match the optical thickness derived from MODIS. This means that there will be more uncertainties in multilayer situations where the CALIOP signal is attenuated before reaching the lower layers. In this case, the scaling of MODIS optical thickness will still retain the radiative impact of the total cloud column, but the cloud layers below the attenuation level will be missed from the vertical distribution of condensate. We therefore expect some underestimation in the frequency of occurrence of CVSs with clouds in all three layers, in favor of those with clouds in the H and M layers. This reinforces the role of clouds with tops in the lower and midlevel layers.

In section 2c, we have estimated the fraction of clouds with supercooled liquid tops from three different methods. For the range of temperatures between −40° and 0°C, this fraction is between 60% for method 3 and 84% for method 2, with the standard method giving a value of 80%. Figure 3a shows that the contribution of each CVS to the total shortwave reflected flux (color bars) is very well correlated with its frequency of occurrence (gray bars). We use this fact and the super-cooled liquid fractions from the three methods to estimate that clouds with supercooled liquid tops contribute between 23% and 32% of the total reflected flux. Since the partition between mixed-phase and super-cooled liquid is uncertain, it is probably more robust to add the SCL and MIX categories together. The contribution of both classes goes from 27% to 38%.

The Northern Hemisphere oceans do not show such a large frequency of occurrence of supercooled liquid clouds (Hu et al. 2010; Huang et al. 2012, 2015), which poses the question of what controls the differences in the observed distribution of cloud phase in both hemispheres. The Southern Ocean shows large amounts of cloud liquid water in summer, with average temperatures ranging between −10° and 0°C (Fig. 4). The 0°C isotherm is located much farther poleward over the Northern Hemisphere in summer due to the warmer SSTs for the same latitude band. The Southern Ocean
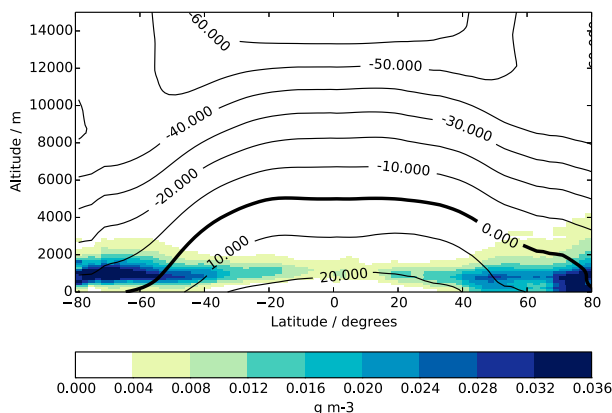

FIG. 4. Ocean-only zonal-mean cross sections of cloud LWC and air temperature. Summer season average in each hemisphere: DJF for the Southern Hemisphere, and JJA for the Northern Hemisphere. LWC is shown in color, and the line contours show the air temperature (°C).

summer lower troposphere stays in a range of temperatures that favors the existence of supercooled liquid clouds. Huang et al. (2015) suggest that the difference in the occurrence of supercooled liquid cloud between the southern and northern ocean midlatitudes in their respective summer seasons is fundamentally controlled by the thermodynamics. We investigate this by comparing the frequency distributions of liquid cloud-top temperatures in the summer season in the midlatitude oceans in both hemispheres (Fig. 5a). We restrict the analysis to ocean points between 50° and 60°S, where the occurrence of supercooled liquid is a maximum in the Southern Hemisphere. Consistent with the zonal mean cross section of cloud liquid water content (Fig. 4), the Northern Hemisphere clouds are warmer than those over the Southern Ocean within the same latitude range. It is also important to notice that the shapes of the distributions are very different, with the Northern Hemisphere distribution being negatively skewed. This may be due to gross thermodynamic structural differences and/or may suggest a possible role of aerosol–cloud interactions in controlling the differences in cloud phase between both hemispheres. It is worth mentioning that the Southern Ocean seems to show smaller values of LWC than the Northern Hemisphere oceans below 500 m. It is not obvious why this difference exists, and it might just be an artifact of the CCCM dataset.

We attempt to remove the influence of the gross thermodynamic difference by imposing the same SST distribution in both hemispheres. We randomly sample cloud-top temperatures such that the populations in both hemispheres have the same underlying SST distribution (Fig. 5b). We impose a constant (top hat) SST distribution in the SST range where the two original
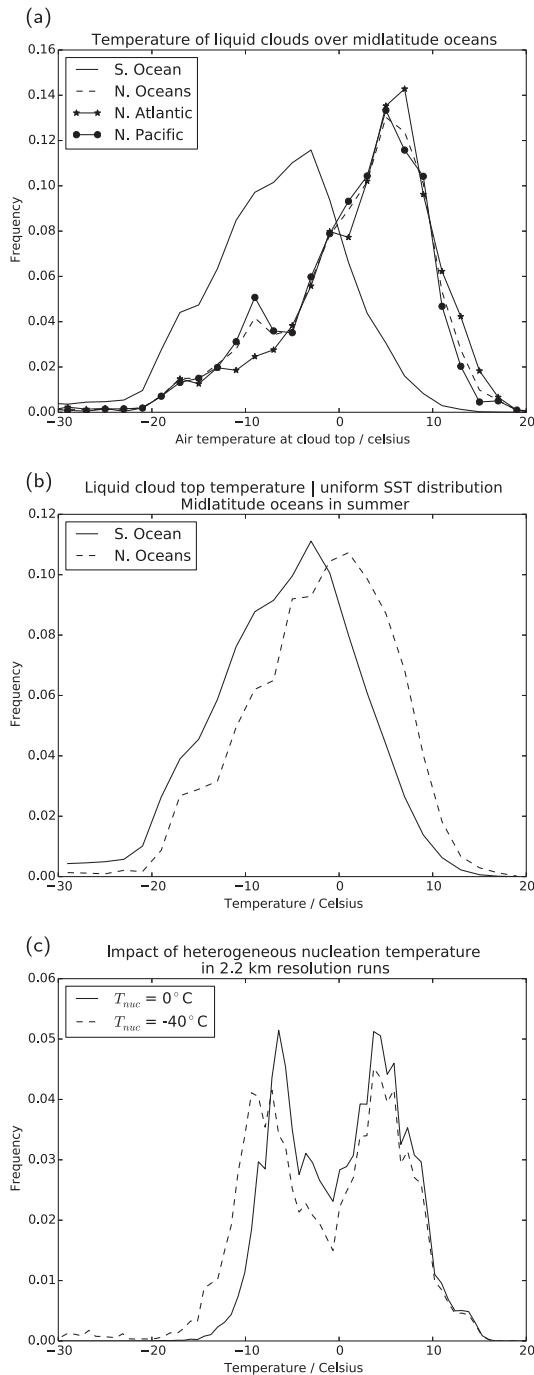
FIG. 5. Hemispheric difference of cloud-top temperature distributions. Normalized frequency distributions of liquid cloud-top temperatures. Only points with liquid cloud tops in the uppermost layer are included. The distributions are calculated by sampling midlatitude ocean points between 50° and 60° latitude in summer, for the Southern Ocean during DJF and Northern Hemisphere basins during JJA. (a) Distributions from the entire CCCM population. (b) Distributions obtained by random sampling imposing a uniform SST distribution. (c) Distributions from the 2.2-km resolution model simulations with heterogeneous ice nucleation threshold temperatures of 0° (solid) and −40°C (dashed). In (c), liquid cloud top is defined to be the maximum height at which the LWC is greater than or equal to 10^{-5} kg kg^{-1}.

distributions overlap, between 0° and 10°C. The large skewness in the Northern Hemisphere distribution of CTTs disappears, and both hemispheres show a very similar shape. However, the distribution in the Southern Hemisphere is still shifted to colder temperatures by 4°C. A two-tailed Student's t test shows that the means of these two distributions are not equal at a 0.01 level of significance.

Although gross thermodynamic differences (characterized here by the distribution of local SSTs) explain a large part of the differences between both hemispheres, there are other processes that may contribute to the interhemispheric differences. As mentioned above, one possible candidate is the role of aerosol–cloud interactions, driven by the large interhemispheric differences in the amount and composition of aerosols. The Southern Ocean is a pristine environment, with small amounts of dust that can act as ice nuclei (Choi et al. 2010). This limitation in ice nuclei over the Southern Ocean may contribute to enhancing the population of supercooled clouds for the same temperature range. We assess this by studying the sensitivity to ice nucleation of model clouds in the 2.2-km-resolution simulations of a Southern Ocean cyclone described in section 2d (Fig. 5c). We choose a case that contains a midlatitude cyclone in the Southern Ocean, as previous studies have shown that these systems contain clouds that contribute to the Southern Ocean shortwave bias (Bodas-Salcedo et al. 2014). The purpose of this experiment is to demonstrate the effects on liquid and ice water content of limiting the amount of heterogeneous ice nucleation, and therefore we do not present here an evaluation of the simulations against observations.

The histograms of liquid cloud-top temperature show a bimodal distribution. For $T_{\text{nuc}} = 0$°C (solid line), the cold mode peaks around −7°C, indicative of the temperature range of the boundary layer clouds in the simulations. For $T_{\text{nuc}} = -40$°C (dashed line), the tail of the histogram is shifted a few degrees toward colder temperatures, showing that colder liquid cloud-tops are more prevalent if ice nucleation is inhibited. The fraction of grid points with cloud top below 8.4 km that has liquid water cloud top colder than −10°C increase from 0.12 for $T_{\text{nuc}} = 0$°C to 0.28 for $T_{\text{nuc}} = -40$°C. The frequency of points with liquid clouds at −10°C is increased by a factor of 3. Since the total number of points that go into the calculations of the normalized distributions is only 10% larger for $T_{\text{nuc}} = -40$°C, large differences in the frequency for a given temperature imply large differences in the number of liquid clouds. The small increase in the total number of points contributes to explaining the reduction in frequency of the warm mode. The shift of the supercooled liquid mode is

consistent with the observational results in Fig. 5b. The value $T_{nuc} = -40°C$ may be considered an extreme perturbation, but for this case study the top of layer clouds with supercooled water in the cold sector of the cyclone only reach up to $-10°C$ as a result of the subsidence in this sector of the cyclone. It is worth noting that, in the real world, *CALIPSO* reports supercooled liquid down to $-25°C$ near the warm front. Despite that both simulations have trouble producing supercooled liquid water as compared to *CALIPSO*, the effect of limiting the amount of heterogeneous ice nucleation is consistent with the interhemispheric differences shown in Fig. 5b. Setting the freezing temperature to $-20°C$ or even $-10°C$ makes only small differences to the character of the results. The frontal clouds that have cloud tops extending to much colder levels are not affected and are glaciated down to the melting level. Therefore the effects of changing the heterogeneous freezing temperature will largely be seen on the frequency of occurrence of supercooled liquid water at these temperatures rather than seeing large frequencies of occurrence at much colder temperatures.

This modeling evidence suggests that microphysical processes also play a role in the observed interhemispheric differences of supercooled liquid clouds. However, our characterization of the thermodynamic state is very basic. For instance, although we have restricted this analysis to ocean points, the Northern Hemisphere contains large areas of land that not only impact the aerosol distribution, but also the vertical thermodynamic structure of air advected over the oceans that cannot be fully captured by the underlying SSTs. Therefore, more needs to be done to disentangle the thermodynamic, dynamic, and microphysical contributions to the observed interhemispheric differences in cloud phase.

Since the physical processes that control cloud phase are poorly represented in models, the results presented here may have consequences for climate simulations. It is also worth noting that, even if models are able to reproduce the observed distribution of cloud condensate, the correct simulation of cloud phase is also important, as liquid clouds are brighter than ice clouds for a given water path. We analyze results from 23 atmosphere-only climate models (see section 2d for details). We compare the DJF reflected shortwave radiation from the AMIP experiment against observations from the CERES-EBAF climatology (Fig. 6). The ensemble shows a strong negative bias between 60° and 70°S, where the amount of supercooled liquid cloud is a maximum in the observations. In this region, a majority of models (gray shading) show a deficit in reflected shortwave radiation. It is also noticeable that the Southern Ocean is the region where the models show larger spread. Previous
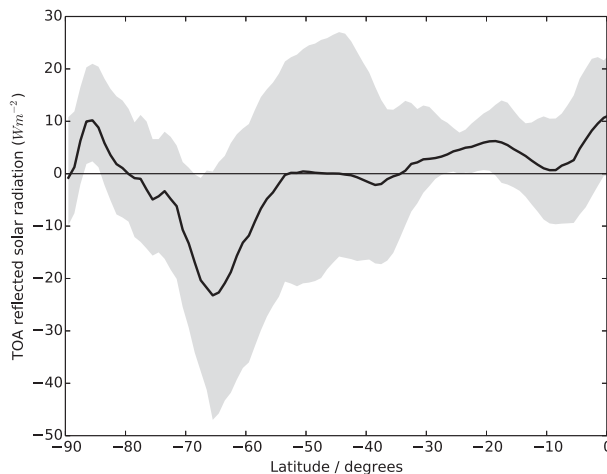

FIG. 6. TOA SW reflected flux error from the CMIP5 AMIP experiments with respect to CERES-EBAF, showing zonal-mean averages for austral summer (DJF). The solid line shows the ensemble-mean bias, and the gray-shaded envelope shows the 10th–90th percentile range.

work has shown that clouds in the cold-air side of cyclones are mainly responsible for these biases (Bodas-Salcedo et al. 2014). Cyclone composite analysis of the CCCM cloud-top phase data shows that this area of the cyclone composite contains large amounts of supercooled liquid clouds (Fig. 7). The poleward side of the cyclones is still dominated by clouds with ice tops. However, the total condensate in the poleward side is not dominated by ice, with the average liquid water path being similar or larger than the ice water path (Figs. 8a and 9a). This suggests that the liquid phase probably dominates the contribution to the TOA shortwave flux in this region of the cyclones.

Figures 8 and 9 also show model composites of cloud liquid and ice water path. Only a subset of the 23 models included in Fig. 6 submitted the necessary daily diagnostics to do the cyclone composite analysis. Models tend to show a very poor representation of cloud liquid water path (LWP) (Fig. 8). Half of the models tend to underestimate cloud LWP in the cold-air region of the cyclone composites. The models that show less LWP in the cold sector (CNRM-CM5, HadGEM2-A, MIROC5, and MRI-CGCM3) also show the largest shortwave biases [see Fig. 4 in Bodas-Salcedo et al. (2014)]. All the models overestimate cloud LWP in the warm frontal region of the composite, but this has to be interpreted with caution. The observations probably underestimate the amount of cloud liquid water in the warm sector, as this is an area that also contains large quantities of ice clouds above (Figs. 7c and 9a) that will reduce the capability to retrieve cloud liquid content under thick ice clouds. It is worth mentioning that the cyclone
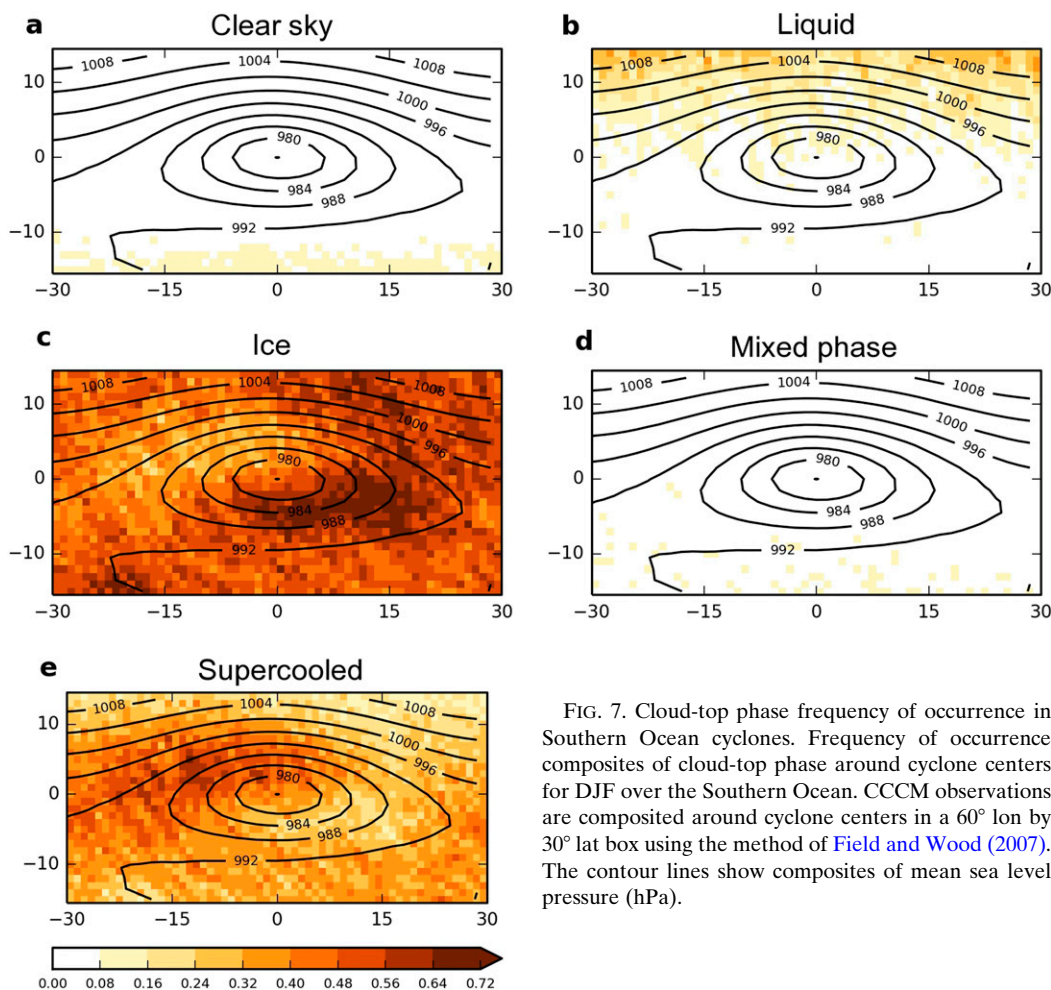
FIG. 7. Cloud-top phase frequency of occurrence in Southern Ocean cyclones. Frequency of occurrence composites of cloud-top phase around cyclone centers for DJF over the Southern Ocean. CCCM observations are composited around cyclone centers in a 60° lon by 30° lat box using the method of Field and Wood (2007). The contour lines show composites of mean sea level pressure (hPa).

compositing does not apply a rotation to align the position of the fronts, which makes a very strict definition of the location of the warm and/or cold sectors not possible. Figure 3 in Bodas-Salcedo et al. (2014) shows a schematic of the approximate position of the warm and cold sectors in the cyclone composite. Roughly speaking, the warm sector occupies the first quadrant (in the standard trigonometrical definition), but it also extends to parts of the other quadrants.

Figure 9 also shows that the models simulation of cloud ice water path is more in line with the observations. They tend to underestimate the ice water path (IWP) in the warm sector, although CCCM may be an overestimate in this region. Some models show too much ice in the cold sector, which may partially compensate for the shortwave biases introduced by the lack of liquid water path. These results show that models have great difficulties in simulating the correct distribution of cloud condensate, and that they may produce a decent climatological TOA shortwave radiation budget

due to compensating errors in the distribution of cloud condensate.

Analysis of climate change experiments (not shown) show strong negative shortwave feedbacks in the latitudes where large present-day biases exist. This suggests that the midlatitude shortwave negative cloud–radiative feedbacks observed in models may be overestimated due to a poor simulation of supercooled liquid clouds in the present day, with potential implications for our current estimates of climate sensitivity. A detailed analysis of the cloud responses in these climate change experiments is under way and will be reported elsewhere.

4. Conclusions

We have carried out a comprehensive analysis of the role of clouds in the solar radiation budget over the Southern Ocean. We have used satellite data from the latest generation of passive and active instruments, and
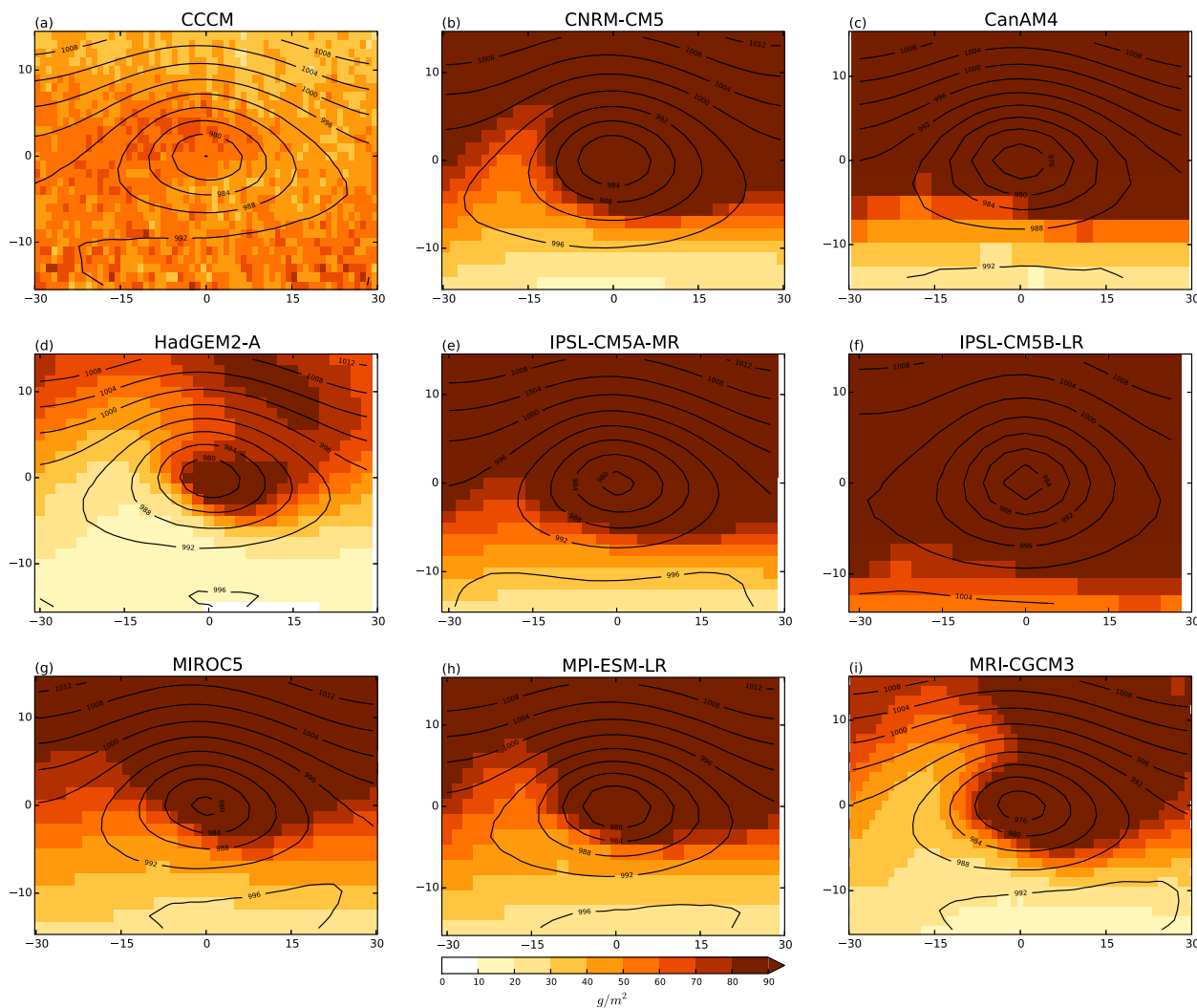
Liquid Water Path

FIG. 8. LWP around cyclone centers over the Southern Ocean in austral summer (DJF). Cyclone composites calculated using the method of Field and Wood (2007): (a) CCCM data and (b)–(i) CMIP5 AMIP experiments.

radiative transfer simulations to quantify the contribution of different cloud types and cloud thermodynamic phase to the TOA radiation budget. We focus our analysis on the austral summer as the main aim of this study is in the solar part of the spectrum. The methodology presented here can be easily extended to the entire globe and to the longwave part of the spectrum.

This analysis shows that scenes where the uppermost cloud layer contains supercooled liquid water contribute between 27% and 38% to the total amount of shortwave reflected radiation in the 40°–70°S region. We have investigated the drivers of the differences in the frequency of occurrence of supercooled liquid between hemispheres in their respective summers, and our results

suggest that differences in the thermodynamics of the environment explain most of the differences, consistent with the findings of previous studies. Other processes, like ice nucleation, seem to play a secondary role, at least during the summer months. These results show that a better simulation of supercooled liquid clouds is crucial for a better representation of the TOA radiation budget over the Southern Ocean, consistent with the recent modeling study by Kay et al. (2016).

We apply cyclone compositing techniques to CMIP5 model data to understand the implications of these findings in the context of present-day climate simulations over the Southern Ocean. The poor simulation of supercooled liquid clouds in climate models is shown to
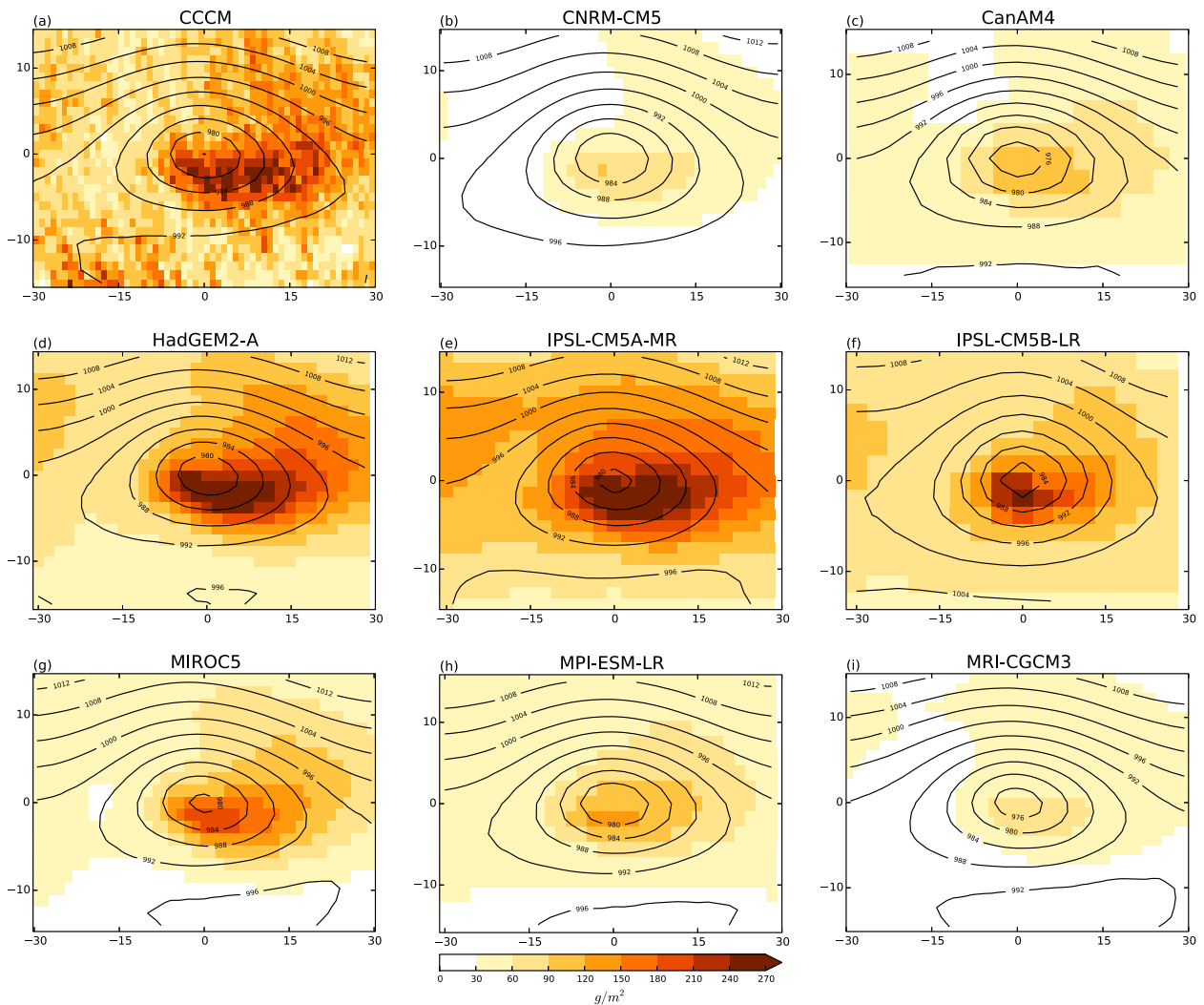
Ice Water Path

FIG. 9. As in Fig. 8, but for IWP.

lead to significant model errors. Models that show large shortwave errors in the cold-air region of the cyclone composites tend to underestimate cloud LWP in that region of the cyclone composite, where the observations generally show a large frequency of occurrence of clouds with supercooled liquid tops exposed to space. Previous studies have shown that this area of the cyclones is responsible for the Southern Ocean solar radiation biases (Bodas-Salcedo et al. 2014). Some models show too much ice in the cold sector, which may partially compensate for the shortwave biases introduced by the lack of liquid water path. These results show that models have great difficulties in simulating the correct distribution of cloud condensate, and that they may produce a decent climatological TOA shortwave (SW) radiation budget due to compensating errors in the spatial distribution of cloud condensate. To connect these results more directly with parameterization errors, more work needs to be done to implement model diagnostics that are directly comparable with the results presented here.

These results may undermine our confidence in the large negative cloud feedbacks found in climate change simulations over the Southern Ocean. Future work should focus on the potential implication of these findings in these large negative feedbacks. It is also important to coordinate efforts (field campaigns, analysis of remote sensing data, and detailed modeling) if we want to advance our knowledge of the physical processes that control the formation and evolution of supercooled liquid clouds over the Southern Ocean and to increase our confidence in simulated cloud feedbacks.

REFERENCES

Abel, S. J., D. N. Walters, and G. Allen, 2010: Evaluation of stratocumulus cloud prediction in the Met Office forecast model during VOCALS-REx. *Atmos. Chem. Phys.*, **10**, 10 541–10 559, doi:10.5194/acp-10-10541-2010.

Baran, A. J., P. Field, K. Furtado, J. Manners, and A. Smith, 2013: A new high- and low-frequency scattering parameterization for cirrus and its impact on a high-resolution numerical weather prediction model. *AIP Conf. Proc.*, Berlin, Germany, American Institute of Physics, 716–719, doi:10.1063/1.4804870.

Bennartz, R., and Coauthors, 2013: July 2012 Greenland melt extent enhanced by low-level liquid clouds. *Nature*, **496**, 83–86, doi:10.1038/nature12002.

Bloom, S. C., A. da Silva, and D. Dee, 2005: Documentation and validation of the Goddard Earth Observing System (GEOS) Data Assimilation System version 4. NASA Tech. Memo. 104606, Vol. 26, 187 pp.

Bodas-Salcedo, A., K. D. Williams, P. R. Field, and A. P. Lock, 2012: The surface downwelling solar radiation surplus over the Southern Ocean in the Met Office model: The role of midlatitude cyclone clouds. *J. Climate*, **25**, 7467–7486, doi:10.1175/JCLI-D-11-00702.1.

——, and Coauthors, 2014: Origins of the solar radiation biases over the Southern Ocean in CFMIP2 models. *J. Climate*, **27**, 41–56, doi:10.1175/JCLI-D-13-00169.1.

Ceppi, P., Y.-T. Hwang, D. M. W. Frierson, and D. L. Hartmann, 2012: Southern Hemisphere jet latitude biases in CMIP5 models linked to shortwave cloud forcing. *Geophys. Res. Lett.*, **39**, L19708, doi:10.1029/2012GL053115.

Cesana, G., J. E. Kay, H. Chepfer, J. M. English, and G. de Boer, 2012: Ubiquitous low-level liquid-containing Arctic clouds: New observations and climate model constraints from *CALIPSO*-GOCCP. *Geophys. Res. Lett.*, **39**, L20804, doi:10.1029/2012GL053385.

Choi, Y.-S., R. S. Lindzen, C.-H. Ho, and J. Kim, 2010: Space observations of cold-cloud phase change. *Proc. Natl. Acad. Sci. USA*, **107**, 11 211–11 216, doi:10.1073/pnas.1006241107.

Edwards, J. M., and A. Slingo, 1996: Studies with a flexible new radiation code. I: Choosing a configuration for a large-scale model. *Quart. J. Roy. Meteor. Soc.*, **122**, 689–720, doi:10.1002/qj.49712253107.

Field, P. R., and R. Wood, 2007: Precipitation and cloud structure in midlatitude cyclones. *J. Climate*, **20**, 233–254, doi:10.1175/JCLI3998.1.

Forbes, R. M., and M. Ahlgrimm, 2014: On the representation of high-latitude boundary layer mixed-phase cloud in the ECMWF global model. *Mon. Wea. Rev.*, **142**, 3425–3445, doi:10.1175/MWR-D-13-00325.1.

Gates, W., 1992: AMIP: The Atmospheric Model Intercomparison Project. *Bull. Amer. Meteor. Soc.*, **73**, 1962–1970, doi:10.1175/1520-0477(1992)073<1962:ATAMIP>2.0.CO;2.

Gregory, D., and D. Morris, 1996: The sensitivity of climate simulations to the specification of mixed phase clouds. *Climate Dyn.*, **12**, 641–651, doi:10.1007/BF00216271.

Grosvenor, D. P., and R. Wood, 2014: The effect of solar zenith angle on MODIS cloud optical and microphysical retrievals within marine liquid water clouds. *Atmos. Chem. Phys.*, **14**, 7291–7321, doi:10.5194/acp-14-7291-2014.

Haynes, J. M., T. H. Vonder Haar, T. L'Ecuyer, and D. Henderson, 2013: Radiative heating characteristics of Earth's cloudy atmosphere from vertically resolved active sensors. *Geophys. Res. Lett.*, **40**, 624–630, doi:10.1002/grl.50145.

Hogan, R. J., P. N. Francis, H. Flentje, A. J. Illingworth, M. Quante, and J. Pelon, 2003: Characteristics of mixed-phase clouds. I: Lidar, radar and aircraft observations from CLARE'98. *Quart. J. Roy. Meteor. Soc.*, **129**, 2089–2116, doi:10.1256/rj.01.208.

Hu, Y., S. Rodier, K. Xu, W. Sun, J. Huang, B. Lin, P. Zhai, and D. Josset, 2010: Occurrence, liquid water content, and fraction of supercooled water clouds from combined CALIOP/IIR/MODIS measurements. *J. Geophys. Res.*, **115**, D00H34, doi:10.1029/2009JD012384.

Huang, Y., S. T. Siems, M. J. Manton, A. Protat, and J. Delanoë, 2012: A study on the low-altitude clouds over the Southern Ocean using the DARDAR-MASK. *J. Geophys. Res.*, **117**, D18204, doi:10.1029/2012JD017800.

——, A. Protat, S. T. Siems, and M. J. Manton, 2015: A-Train observations of maritime midlatitude storm-track cloud systems: Comparing the Southern Ocean against the North Atlantic. *J. Climate*, **28**, 1920–1939, doi:10.1175/JCLI-D-14-00169.1.

Hwang, Y.-T., and D. M. W. Frierson, 2013: Link between the double-Intertropical Convergence Zone problem and cloud biases over the Southern Ocean. *Proc. Natl. Acad. Sci. USA*, **110**, 4935–4940, doi:10.1073/pnas.1213302110.

Kato, S., S. Sun-Mack, W. F. Miller, F. G. Rose, Y. Chen, P. Minnis, and B. A. Wielicki, 2010: Relationships among cloud occurrence frequency, overlap, and effective thickness derived from *CALIPSO* and *CloudSat* merged cloud vertical profiles. *J. Geophys. Res.*, **115**, D00H28, doi:10.1029/2009JD012277.

——, and Coauthors, 2011: Improvements of top-of-atmosphere and surface irradiance computations with *CALIPSO*-, *CloudSat*-, and MODIS-derived cloud and aerosol properties. *J. Geophys. Res.*, **116**, D19209, doi:10.1029/2011JD016050.

Kay, J. E., C. Wall, V. Yettella, B. Medeiros, C. Hannay, P. Caldwell, and C. Bitz, 2016: Global climate impacts of fixing the Southern Ocean shortwave radiation bias in the Community Earth System Model (CESM). *J. Climate*, doi:10.1175/JCLI-D-15-0358.1, in press.

Kristjánsson, J. E., J. M. Edwards, and D. L. Mitchell, 1999: A new parameterization scheme for the optical properties of ice crystals for use in general circulation models of the atmosphere. *Phys. Chem. Earth*, **24B**, 231–236, doi:10.1016/S1464-1909(98)00043-4.

L'Ecuyer, T. S., N. B. Wood, T. Haladay, G. L. Stephens, and P. W. Stackhouse, 2008: Impact of clouds on atmospheric heating

based on the R04 CloudSat fluxes and heating rates data set. *J. Geophys. Res.*, **113**, D00A15, doi:10.1029/2008JD009951.

Loeb, N. G., S. Kato, K. Loukachine, and N. Manalo-Smith, 2005: Angular distribution models for top-of-atmosphere radiative flux estimation from the Clouds and the Earth's Radiant Energy System instrument on the *Terra* satellite. Part I: Methodology. *J. Atmos. Oceanic Technol.*, **22**, 338–351, doi:10.1175/JTECH1712.1.

——, B. A. Wielicki, D. R. Doelling, S. Kato, T. Wong, G. L. Smith, D. F. Keyes, and N. Manalo-Smith, 2009: Toward optimal closure of the Earth's top-of-atmosphere radiation budget. *J. Climate*, **22**, 748–766, doi:10.1175/2008JCLI2637.1.

Marchand, R., G. G. Mace, T. Ackerman, and G. L. Stephens, 2008: Hydrometeor detection using *CloudSat*—An Earth-orbiting 94-GHz cloud radar. *J. Atmos. Oceanic Technol.*, **25**, 519–533, doi:10.1175/2007JTECHA1006.1.

Minnis, P., and Coauthors, 2011: CERES edition-2 cloud property retrievals using TRMM VIRS and Terra and Aqua MODIS data—Part I: Algorithms. *IEEE Trans. Geosci. Remote Sens.*, **49**, 4374–4400, doi:10.1109/TGRS.2011.2144601.

Rienecker, M. M., and Coauthors, 2008: The GEOS-5 Data Assimilation System—Documentation of versions 5.0.1 and 5.1.0, and 5.2.0. NASA Tech Rep. NASA/TM-2008-104606, 97 pp.

Rossow, W. B., and R. A. Schiffer, 1999: Advances in understanding clouds from ISCCP. *Bull. Amer. Meteor. Soc.*, **80**, 2261–2287, doi:10.1175/1520-0477(1999)080<2261:AIUCFI>2.0.CO;2.

Senior, C. A., and J. F. B. Mitchell, 1993: Carbon dioxide and climate: The impact of cloud parameterization. *J. Climate*, **6**, 393–418, doi:10.1175/1520-0442(1993)006<0393:CDACTI>2.0.CO;2.

Stephens, G. L., and Coauthors, 2002: The *CloudSat* mission and the A-Train. *Bull. Amer. Meteor. Soc.*, **83**, 1771–1790, doi:10.1175/BAMS-83-12-1771.

Taylor, K. E., R. J. Stouffer, and G. A. Meehl, 2012: An overview of CMIP5 and the experiment design. *Bull. Amer. Meteor. Soc.*, **93**, 485–498, doi:10.1175/BAMS-D-11-00094.1.

Tselioudis, G., W. Rossow, Y. Zhang, and D. Konsta, 2013: Global weather states and their properties from passive and active satellite cloud retrievals. *J. Climate*, **26**, 7734–7746, doi:10.1175/JCLI-D-13-00024.1.

Tsushima, Y., and Coauthors, 2006: Importance of the mixed-phase cloud distribution in the control climate for assessing the response of clouds to carbon dioxide increase: A multi-model study. *Climate Dyn.*, **27**, 113–126, doi:10.1007/s00382-006-0127-7.

Williams, K. D., and M. J. Webb, 2009: A quantitative performance assessment of cloud regimes in climate models. *Climate Dyn.*, **33**, 141–157, doi:10.1007/s00382-008-0443-1.

——, and Coauthors, 2013: The Transpose-AMIP II experiment and its application to the understanding of Southern Ocean cloud biases in climate models. *J. Climate*, **26**, 3258–3274, doi:10.1175/JCLI-D-12-00429.1.

Wilson, D. R., and S. P. Ballard, 1999: A microphysically based precipitation scheme for the UK Meteorological Office Unified Model. *Quart. J. Roy. Meteor. Soc.*, **125**, 1607–1636, doi:10.1002/qj.49712555707.

Winker, D. M., M. A. Vaughan, A. Omar, Y. Hu, K. A. Powell, Z. Liu, W. H. Hunt, and S. A. Young, 2009: Overview of the *CALIPSO* mission and CALIOP data processing algorithms. *J. Atmos. Oceanic Technol.*, **26**, 2310–2323, doi:10.1175/2009JTECHA1281.1.